Design and optimization of GaAs/AlGaAs heterojunction infrared detectors

D. G. Esaev,[a] M. B. M. Rinzan, S. G. Matsik, and A. G. U. Perera
Department of Physics and Astronomy, Georgia State University, Atlanta, Georgia 30303

(Received 11 March 2004; accepted 25 June 2004)

Design, modeling, and optimization principles for GaAs/AlGaAs heterojunction interfacial workfunction internal photoemission (HEIWIP) infrared detectors for a broad spectral region are presented. Both *n*-type and *p*-type detectors with a single emitter or multiemitters, grown on doped and undoped substrates are considered. It is shown that the absorption, and therefore responsivity, can be increased by optimizing the device design. Both the position and the strength of the responsivity peaks can be tailored by varying device parameters such as doping and the thickness. By utilizing a resonant cavity architecture, the effect of a buffer layer on the response is discussed. Model results, which are in good agreement with the experimental results, predict an optimized design for a detector with a peak response of 9 A/W at 26 μm with a zero response threshold wavelength $\lambda_0=100$ μm. For a $\lambda_0=15$ μm HEIWIP detector, background limited performance temperature (BLIP temperature), for 180° field of view (FOV) is expected around 80 K. For a $\lambda_0=70$ μm optimized design, a highly doped *n*-type substrate could increase the peak detectivity from 1.7×10^{10} to 3.4×10^{10} Jones at a FOV=180° operated at temperatures below $T<T_{\mathrm{BLIP}}=13$ K. Intrinsic response times on the order of picoseconds are expected for these detectors. © *2004 American Institute of Physics*. [DOI: 10.1063/1.1786342]

I. INTRODUCTION

High performance far-infrared (up to 600 μm) semiconductor detectors are in demand for space astronomy applications, such as European Space Agency's Herschel Space Observatory (formerly known as the "far infrared and submillimetre telescope"—FIRST) program.[1] The recent successful development of quantum cascade lasers[2] opens the possibility of specialized optical communication in the wavelength range up to 25 μm, requiring highly sensitive and fast detectors. Present far-infrared (FIR) terahertz detectors in use or under development for this wavelength range are extrinsic Ge photoconductors (stressed or unstressed),[3] and Ge,[4] and Si[5] blocked impurity band detectors.

The advantages of the heterojunction interfacial workfunction internal photoemission (HEIWIP) detectors are the zero response threshold wavelength λ_0 tailorability, and the detectivity in a wide wavelength range.[6–8] The material advantage of GaAs/AlGaAs provides an excellent uniformity and large arrays.[9] The basic structure of a HEIWIP detector consists of a top contact (p^{++} or n^{++}) layer, several periods of undoped barrier and (p^{+} or n^{+}) emitter layers, and a bottom (p^{++} or n^{++}) contact. The detection mechanism involves free carrier absorption in the emitter layer, followed by the internal photoemission of photoexcited carriers across the junction barrier, and then collection. The λ_0 is determined by the interfacial workfunction Δ between the emitter and the barrier. By adjusting the Al fraction in the barrier λ_0 can be tailored to any desired wavelength. It was shown that varying the Al fraction in the barrier from 2% to 0.5% varies λ_0 from 65 to 92 μm.[7]

The main mechanism governing the operation of these detectors is the photon absorption by free carriers in the emitter. An effective way to increase absorption, and thereby the responsivity, especially for shorter wavelength devices, is to use the resonant cavity architecture in the structure.[10] An optimal combination of *n*-type and *p*-type layers, with specific doping concentrations and thicknesses, enhances the optical electric field in the emitter, and photon absorption as a result. The BLIP temperature and the detectivity D^* of the detector depend on the dark current mechanism and responsivity, while hot carrier relaxation and transport processes in the emitter determine the responsivity and response time. Here, the principles of design for optimizing the performance of GaAs/AlGaAs HEIWIP IR detectors considering different types of layers and different spectral regions are presented.

II. MODEL DESCRIPTION

A. Light propagation in the structure

A typical HEIWIP detector structure is shown in Fig. 1. The workfunction consists of two contributions: (i) the band gap offset due to the difference in Al fraction between the emitter and barrier Δ_x, and (ii) the band gap narrowing due to the doping in the emitter layers Δ_d, giving $\Delta=\Delta_x+\Delta_d$ as shown in Fig. 2. Here, Δ_d does not vary significantly with doping for N_A in the range $1-8\times10^{18}$ cm^{-3} while Δ_x can be varied by adjusting the Al fraction of the emitters and barriers.

The radiation propagation in the structure may be described by introducing the complex refractive index n_j and complex permittivity ε_j [according to $n_j=\sqrt{\varepsilon_j(\omega)}$] of the jth layer in the structure. For polar materials like GaAs, permittivity has two terms describing the interaction of incident radiation of frequency ω with the free carriers in accordance with the Drude model, and with the optical phonons:[11]

[a]Permanent address: Institute of Semiconductor Physics, Siberian Branch of the RAS, Novosibirsk, 630090 Russia.

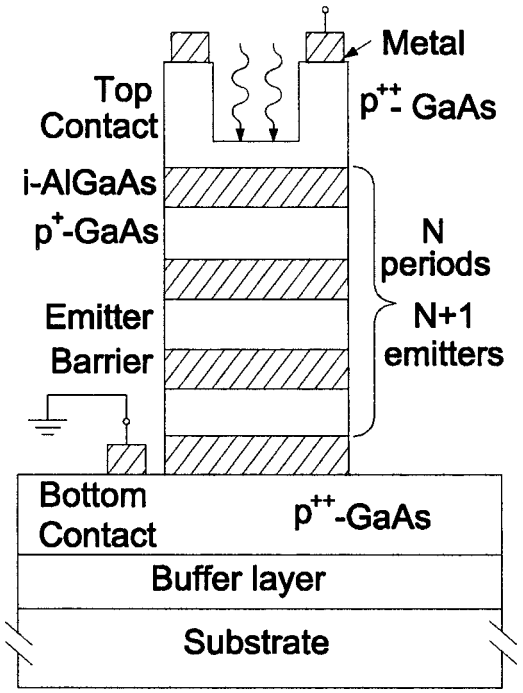

FIG. 1. The structure of a typical *p*-GaAs HEIWIP detector after processing. p^{++}, p^{+}, and *i*-AlGaAs are the contact, emitter, and barrier, respectively. The structure may have single emitter or several emitter/barrier junctions. The substrate may be doped (*n* or *p* type) or semi-insulating. *N* is the number of periods, giving $N+1$ emitters.

$$\varepsilon_j(\omega) = \varepsilon_{\infty,j}\left[1 - \frac{\omega_{p,j}^2}{\omega(\omega + i\omega_{0,j})}\right] + \frac{\omega_{\mathrm{TO},j}^2(\varepsilon_{s,j} - \varepsilon_{\infty,j})}{\omega_{\mathrm{TO},j}^2 - \omega^2 - i\omega\gamma_j}. \quad (1)$$

Here, ε_s and ε_∞ are the static and high frequency dielectric constants of the intrinsic semiconductor, $\omega_0 = 1/\tau$ is the free carrier damping constant, where τ is a relaxation time, ω_{TO} is the transverse optical phonon frequency, and γ is a phonon damping coefficient. The plasma frequency of free carriers with effective mass m^* and concentration N_p is $\omega_p = \sqrt{N_p q^2/\varepsilon_o \varepsilon_\infty m^*}$, where q is the magnitude of the electron charge.

The transfer matrix method was used to calculate the transmittance $\mathcal{T}$ and reflectance $\mathcal{R}$ of the structures.[12,13] Total absorption was calculated as the difference between unity and the sum of the reflectance and transmittance $\mathcal{A} = 1 - \mathcal{T} - \mathcal{R}$.

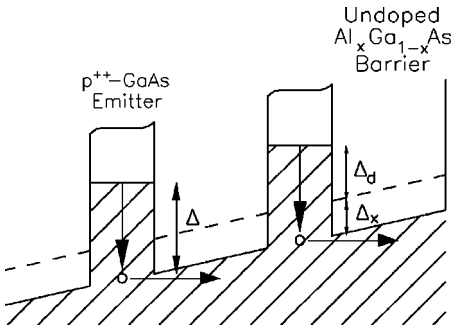

FIG. 2. Partial band diagram of the active region of a HEIWIP detector using doped GaAs as the emitter and undoped $Al_xGa_{1-x}As$ as the barrier, showing the contributions to the workfunction from the band gap narrowing Δ_d and the GaAs/$Al_xGa_{1-x}As$ offset Δ_x. The dashed line indicates the location of the valence band edge in the barrier if it were GaAs. The Al fraction is indicated by *x*.

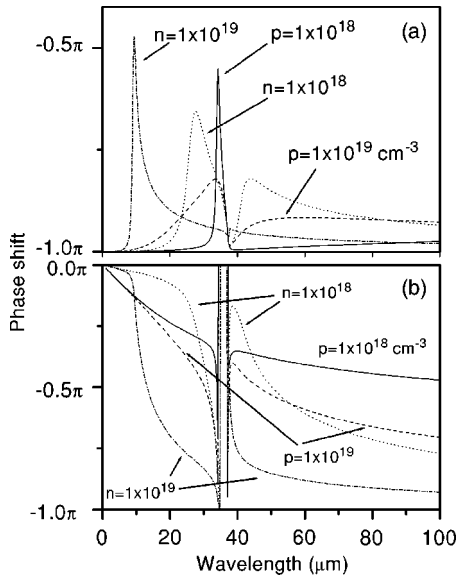

FIG. 3. Phase shift variation of the reflected wave with wavelength for *n*- and *p*-type GaAs with doping concentrations of 1×10^{18} and 1×10^{19} cm^{-3}, (a) reflection from the vacuum/*n* (or *p*)-GaAs interface, (b) reflection from the undoped GaAs/*n* (or *p*)-GaAs interface.

The effective depth of radiation penetration into the layers, skin depth $\delta(\omega)$, which depends on the wavelength, doping concentration *N*, and effective mass of the free carriers can be written as $\delta(\omega) = c/[\omega\,\mathrm{Im}(n(\omega, N))]$. The skin depth has a strong dependence for short wavelengths while saturating at longer wavelengths. Hence, a thin emitter layer will be almost transparent to shorter wavelengths without any appreciable absorption, providing a negligible contribution to the photo current.

For a given wavelength and doping concentration, an *n*-doped layer has a smaller skin depth due to lower effective mass of electrons, resulting in higher reflectivity than for a *p*-doped layer. Therefore, *n*-doped layers could be used as mirrors inside the structure allowing wavelength-selective enhancement of photon absorption.

As the formation of standing waves in the structure depends on both the amplitude and the phase, the phase shift of the reflected wave from the incident wave becomes another important parameter in the design process. The variation of phase shift with wavelength for waves reflected from vacuum/doped (*n*- or *p*-type) GaAs interface is shown in Fig. 3(a). The doped GaAs layers are assumed to be adequately thick, covering several skin depths. This shift is $\approx\pi$ for a wide spectral region except for the narrow region around the resonance optical phonon frequency.

The phase shift variations with wavelength for waves reflected from undoped GaAs/doped (*n*- or *p*-type) GaAs interface for different doping concentrations are shown in Fig. 3(b). Such reflections occur from interfaces inside the structure. As the shift varies over a wide wavelength range, a varying interference condition is produced throughout the spectral range.

B. Responsivity

Responsivity of the photodetector at wavelength λ is given by

$$R = \eta g_p \frac{q}{hc}\lambda, \tag{2}$$

where h is Planck's constant, η is the total quantum efficiency, and g_p is the photoconductive gain.

The responsivity calculations were performed by considering photoexcitation of carriers in the emitter, hot-carrier transport, thermalization, and photoemission into the barrier. Total quantum efficiency[14] is the product of photon absorption η_a, internal photoemission η_i, and hot-carrier transport probabilities η_t, $\eta = \eta_a \eta_i \eta_t$, where η_i is described by an "escape cone" model, and η_t follows the Vickers-Mooney model, and was calculated as in Refs. 15 and 16.

The photon absorption probability η_a is defined as the fraction of the incident photon flux that is absorbed by the free carriers in the emitter and is calculated from the expression

$$\eta_a = 2\frac{\omega}{c}\,\mathrm{Im}[\varepsilon(\omega)]\frac{1}{|E_0|^2}\int_0^W |E(z)|^2 dz$$
$$= 2\frac{\omega}{c}\,\mathrm{Im}[\varepsilon(\omega)]\frac{\overline{|E|^2}}{|E_0|^2}W, \tag{3}$$

where $\mathrm{Im}[\varepsilon(\omega)]$ is the imaginary part of the dielectric function, ω is the wave frequency, $\omega/c = 2\pi/\lambda$ is the wave vector of the incident radiation, E is the electric field of the electromagnetic wave inside the layer, E_0 is the electric field of the incident radiation, and W is the thickness of the emitter layer.

Although the dielectric constant in Eq. (1) contains two additive components, only the first term is included in $\mathrm{Im}[\varepsilon(\omega)]$ in Eq. (3), since only the free carriers that are photoexcited by photons will contribute to the photocurrent. Radiation energy absorbed via optical phonon generation [second term in Eq. (1)] is dissipated in the crystal lattice, producing no hot carriers, and therefore does not contribute to the photocurrent. On the other hand, the value of η_a is proportional to the mean square of the optical electric field $\overline{|E|^2}$, which is formed by the crystal polarization due to both free carriers and the lattice polarization, in the structure. Hence, calculating the electric field distribution across the structure was done by taking both the free carrier and the optical phonon contributions to the permittivity into account.[13]

According to Eq. (3), absorption probability is proportional to the imaginary part of the permittivity. For an n-type layer, the permittivity at wavelengths longer than 8 μm is nearly ten times higher than p type for doping concentrations of $\sim 10^{19}$ cm^{-3}. Therefore, n-type GaAs emitters are more effective for increasing the absorption than p-type emitters. However, the responsivity depends not only on the absorption, but also on the internal photoemission quantum efficiency η_i.

In the escape cone model, η_i is defined as the ratio of the number of excited carriers that have sufficient kinetic energy, associated with the momentum component normal to the interface, to overcome the barrier to the total number of excited carriers. This ratio depends on the Fermi level in the emitter and is different for electrons and holes with similar carrier concentration. The comparison for η_i in n-type and p-type materials is presented in Fig. 4. The photoemission is greater for p-type GaAs than for n type, but the difference between them changes with wavelength.

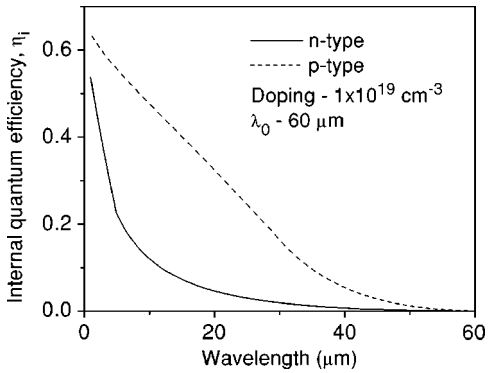

FIG. 4. Internal photoemission quantum efficiency η_i of 100 nm thick n- and p-type GaAs layers with a doping concentration of 1×10^{19} cm^{-3}. For both designs, $\lambda_0 = 60$ μm.

Finally, the transportation of hot carriers is mainly governed by their interactions with phonons and ionized impurities. The strength of such interactions depends on temperature, doping concentration, and the type of carriers. Therefore, the efficiency of the hot-carrier transport η_t, described in terms of the scattering length, is different for electrons and holes.

C. Dark and noise current

Dark current in HEIWIP structures is the sum of both the thermoemission current over the barrier and the tunneling current through the barrier. By increasing the barrier thickness to ~ 0.1 μm and operating at low electric fields ($\leqslant 10^3$ V/cm), the tunneling current could be reduced to a negligible value. The thermionic current in HEIWIP structures, described by the 3D carrier drift model,[17] is given by

$$I_{\mathrm{dark}} = qA\frac{\mu F}{[1+(\mu F/v_{\mathrm{sat}})^2]^{1/2}} 2(m^* kT/2\pi\hbar^2)^{3/2}$$
$$\times \exp[-(\Delta - \alpha F)/kT], \tag{4}$$

where μ is the carrier mobility, F is the electric field, $v_{\mathrm{sat}} \sim 10^7$ cm/s is the saturation drift velocity of the carriers, Δ is the energy gap between the emitter and the barrier due to conduction or valence band offset, and the parameter $\alpha \sim 100-200$ Å determines the effective barrier lowering.

The comparisons of the experimental and calculated [Eq. (4)] dark currents for different temperatures are shown in Fig. 5. Calculations were performed for a HEIWIP detector (sample HE0204) with 16 periods of emitter/barrier layers. The barrier height, $\Delta = 77$ meV, was determined from the Arrhenius plots for the experimental curves at low bias, and was consistent with the experimental λ_0 of 16 μm.[8] The fitting parameter, $\alpha \sim 180$ Å, was used to obtain the fits for the experimental curves. Figure 5 shows that the dark current for HEIWIP structures can be satisfactorily described by the 3D

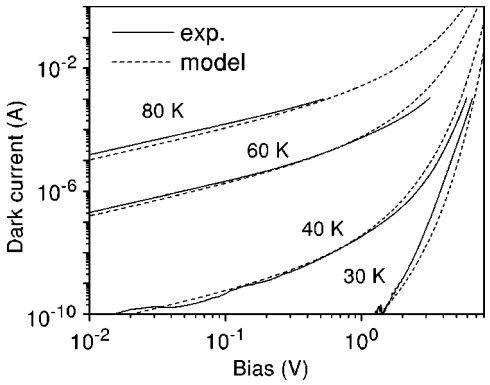

FIG. 5. Experimental and calculated bias dependence of the dark current for HE0204 HEIWIP detector at different operating temperatures. The interfacial workfunction Δ was derived from the Arrhenius plot of the experimental curves. Δ was ~77 meV, and is consistent with λ_0 (Ref. 8).

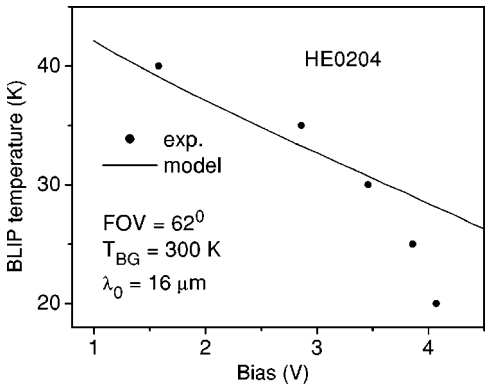

FIG. 6. Experimental and calculated BLIP temperature vs bias curves for sample HE0204. The background temperature was 300 K with a FOV of 62°. λ_0 is 16 μm.

drift model at low bias while the model deviates from experiment for higher biases (above 2.5 V) due to the dominance in tunneling.

The noise current is related to the mean current through the detector $\overline{I}$ by.[18]

$$I_{\text{noise}}^2 = 4q\overline{I}g_n B, \tag{5}$$

where g_n is the noise gain and B is the bandwidth of the measurement. According to Ref. 19, expressions for noise gain g_n and photocurrent gain g_p are

$$g_n = \frac{1-p_c/2}{p_c(N+1)} + \frac{1-(1-p_c)^{N+1}}{p_c(N+1)^2[1-(1-p_c)^N]}, \tag{6}$$

$$g_p = \frac{1}{p_c N}, \tag{7}$$

where p_c is the capture probability of a carrier traversing an emitter and N is the total number of emitters. The ratio g_n/g_p varies from 0.5 to 1 when p_c varies from 0 to 1 and N varies from one to infinity. Therefore, the difference between them may be ignored in many applications. If capture probability is $\ll 1$, there is no difference between noise gain and the photocurrent gain, and they are both given by $1/p_c N$. However, the ratio g_n/g_p approaches $1-p_c/2$ in the limit $N \gg 1$.

The capture probability is defined as $p_c=(1/\tau_{\text{rec}})/(1/\tau_{\text{rec}}+1/\tau_s)=\tau_s/(\tau_s+\tau_{\text{rec}})$, where τ_s is the sweep-out time and τ_{rec} is the recombination time (lifetime). In the case when $\tau_s \ll \tau_{\text{rec}}$, the capture probability p_c is low, and the gain has the conventional expression for photoconductors,

$$g = \tau_{\text{rec}}/N\tau_s = \tau_{\text{rec}}/\tau_{tr} = \mu\tau_{\text{rec}}F/d, \tag{8}$$

where τ_{tr} is transit time, μ is carrier mobility, F is applied electric field, and d is the thickness of the structure. Note that the gain is inversely proportional to the thickness of the structure.

D. Specific detectivity and BLIP regime

Specific detectivity D^* of the detector is defined as

$$D^* = \frac{R\sqrt{A}}{I_{\text{noise}}}, \tag{9}$$

where A is detector area and I_{noise} is the noise current.

In the background limited performance (BLIP) regime, the intrinsic noise of the detector is negligible compared to the noise arising from the fluctuation of the incident background photon flux. As a result, the dark current is lower than the background photocurrent, and the total noise is determined by the photocurrent under the background illumination $\overline{I}=I_{\text{photo}}$. In the detector limited condition, I_{noise} arises mainly from the fluctuation in the number of mobile carriers via generation-recombination (G-R) processes in the emitters, $\overline{I}=I_{\text{dark}}$.

Photocurrent of the detector caused by the background radiation at a temperature T_{BG} and field of view (FOV$=2\theta$) is defined as

$$I_{\text{photo}} = \sin^2(\theta)A\int^{\lambda_0} R(\lambda)\rho(\lambda, T_{\text{BG}})d\lambda, \tag{10}$$

where $\rho(\lambda, T_{\text{BG}})=2\pi c^2 h/\lambda^5[\exp(hc/kT_{\text{BG}})-1]^{-1}$ is Planck's law of radiation.

Experimental and calculated bias dependence of the BLIP temperature for sample HE0204[8] is presented in Fig. 6. Background temperature was $T_{\text{BG}}=300$ K with a FOV of 62°. The experimental and calculated data are in good agreement for bias voltages lower than 3.5 V. The discrepency at higher bias is due to the fact that the 3D drift model for the dark current in HEIWIP detectors is valid only for a low electric field regime. The deviation of measured dark current from the calculated curves can be seen in Fig. 5.

Absorption probability in the structure is approximately (not taking the cavity effect in to consideration) proportional to the total thickness while the gain is inversely proportional. This leads to a responsivity that is independent of thickness and the number of emitters. In the BLIP regime, detectivity is also independent of the thickness, since noise current is dependent only on the background fluctuations. However, the "detector limited noise current" given by Eq. (5) is proportional to the noise gain, which is inversely proportional to the

TABLE I. The architecture of structures under consideration. Top and bottom contacts are highly doped n^{++} GaAs or p^{++} GaAs with a concentration of 1×10^{19} cm^{-3}. Barrier is treated as intrinsic AlGaAs. Substrate is highly doped or semi-insulating (SI) GaAs. Here, W and N show the layer thickness and number of repeated emitter/barrier junctions, respectively. λ_0 is the zero response threshold wavelength. Structures I and II have no additional emitters other than the contact layers while III–V have 28 additional emitters. Structure V has an n-type buffer layer with a doping concentration of 1×10^{19} cm^{-3}. Structure VI has nine periods of emitter/barrier junctions that provide ten emitters. Structure VII has different types of doping for the top and bottom contacts. The experimental results for structures HE0204 and 2409 have been published in Refs. 8 and 13, respectively.

	Top contact		Emitter layer		Barrier layer	Bottom contact		Buffer layer				
Sample No.	Type	W (μm)	Type	W (μm)	W (μm)	Type	W (μm)	Type	W (μm)	Sub	N	λ_0 (μm)
I	n^{++}	0.2	⋯	⋯	0.2 1	n^{++}	0.4- 10	⋯	⋯	SI	⋯	25
II	n^{++}	0.2	⋯	⋯	1	⋯	⋯	⋯	⋯	n^{++}	⋯	25
III	p^{++}	0.2	⋯	⋯	1	p^{++}	0.7	⋯	⋯	SI	28	20
IV	p^{++}	0.2	⋯	⋯	1	⋯	⋯	⋯	⋯	p^{++}	28	20
V	p^{++}	0.2	⋯	⋯	1	p^{++}	0.7	n^{++}	1	SI	28	20
VI	p^{++}	0.4	p^{+}	0.07	0.1	p^{++}	0.7	⋯	⋯	n^{++}	9	15
VII	p^{++}	0.1	p^{+}	0.03	0.05	n^{++}	0.7	⋯	⋯	SI	22	35
HE 0204	p^{++}	0.1	p^{+}	0.019	0.125	p^{++}	0.7	⋯	⋯	SI	16	16
2409	p^{++}	0.2	p^{+}	0.015	0.077	p^{++}	0.73	⋯	⋯	SI	30	70

thickness. Therefore, at temperatures higher than T_{BLIP}, detectivity is higher for thicker structures due to lower gain and lower noise current.

III. RESPONSIVITY SPECTRA

Parameters of structures considered to demonstrate the effects of thickness, doping, and the number of layers on the detector performance are shown in Table I.

Structure I consists of n^{++} top and bottom contacts with an undoped barrier grown on a semi-insulating (SI) GaAs substrate. The total absorption in the structure for a varying bottom contact thickness from 0.4 to 10 μm is presented in Fig. 7(a). The two absorption peaks around 15 and 7 μm are due to the first-and second-order Fabry-Pérot resonance. The position of the resonance peaks can be estimated from the expression for destructive interference between the waves reflected from the top and bottom layers

$$\sum_j \mathrm{Re}[n_j(\lambda)]d_j = (\lambda/4)(2m-1), \quad m=1,2,3,\ldots, \tag{11}$$

where $\mathrm{Re}(n_j)$ is the real part of the refractive index of the jth layer, d_j is the thickness, and the summation is carried through all the layers of the structure.

The intensity of the second-order ($m=2$) peak around 7 μm shows a strong dependence on the bottom contact thickness, because the skin depth at this wavelength is about 10 μm. For a thin bottom contact, most of the incident radiation is transmitted and the second-order peak is weak. When the bottom contact thickness is on the order of skin depth, the first and second absorption peaks are of the same order of magnitude.

The absorption and responsivity of structure I (see Table I) for a barrier thickness of 1 μm, as shown in Figs. 7(a) and 7(b), have the same peak position while for a thinner barrier (0.2 μm) the peak shifts to shorter wavelengths as shown in Fig. 7(c). Forward and reverse response curves refer to photoinjection from the top and bottom contacts, respectively. An interfacial workfunction of $\Delta=50$ meV between the contact layers and the undoped barrier was used in the calculations. The main absorption at the peak wavelengths occurs in the top contact because the maximum optical electric field of the standing wave, about $\lambda/[4\,\mathrm{Re}(n)]\simeq1$ μm from the bot-

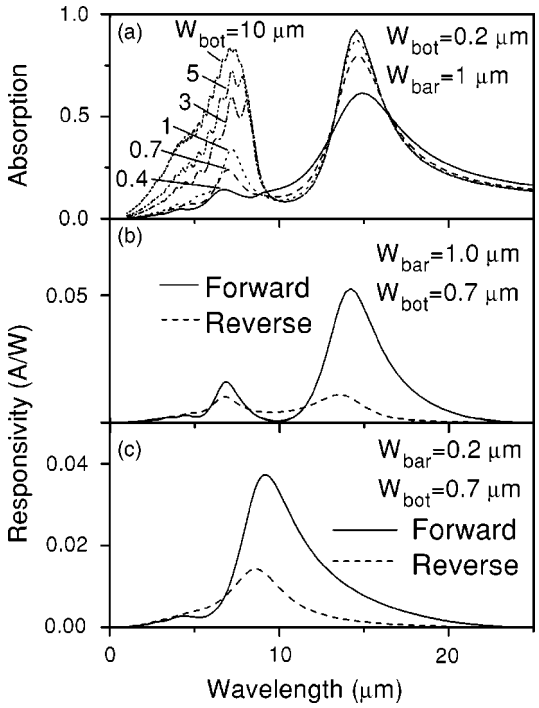

FIG. 7. The calculated (a) absorption and (b and c) responsivity spectra for structure I with n-type top and bottom contacts grown on an undoped substrate for different bottom contact thicknesses. Doping concentration of the contacts is 1×10^{19} cm^{-3}. Thicknesses of the top contact and barrier are $W_{\mathrm{top}}=0.2$ μm and $W_{\mathrm{bar}}=1$ μm, respectively, while bottom contact thickness W_{bot} varies from 0.4 to 10 μm. Responsivity spectra are shown for barrier thicknesses (b) 1 μm and (c) 0.2 μm with a bottom contact thickness of 0.7 μm and $\lambda_0=25$ μm. Forward and reverse implies photoinjection from the top and bottom contacts, respectively.

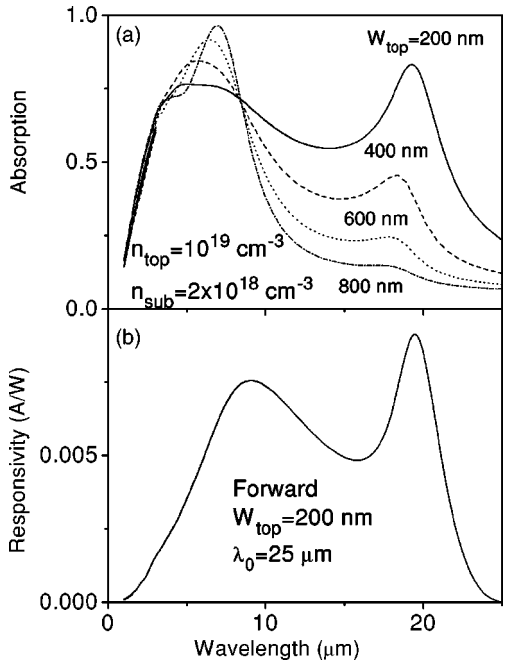

FIG. 8. Calculated total (a) absorption and (b) responsivity for structure II ($\lambda_0 \sim 25$ μm) with different top contact thicknesses. The top contact and substrate are *n* type with doping concentrations of 1×10^{19} and 2×10^{18} cm^{-3}, respectively. The barrier thickness is 1 μm. The forward curve represents photogeneration in the top contact while the reverse curve represents the photogeneration inside the skin depth of the substrate.

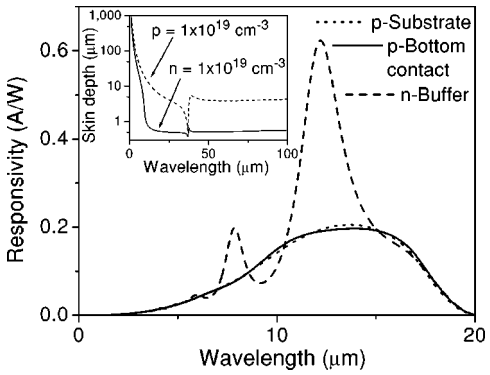

FIG. 9. Calculated responsivity variations for a $\lambda_0=20$ μm detector structure with a 1×10^{19} cm^{-3} doped (i) *p*-bottom contact (structure III), (ii) *p* substrate (structure IV), or (iii) 1 μm thick *n*-buffer layer (structure V) showing the cavity enhancement of the structure with the *n*-type buffer layer. For all three structures the thicknesses of the top contact, bottom contact, and barrier are 200, 700 nm, and 1 μm, respectively. The inset shows skin depth variation for *p*-and *n*-type GaAs. The skin depth for *n*-type GaAs is ~20 times smaller than for *p* type at 12 μm giving a more efficient cavity resonance.

tom contact, falls in the top contact. Hence, the responsivity corresponding to the photogeneration in the top contact is higher than the responsivity from photogeneration in the bottom contact.

It is clear from Fig. 7(c) that the variation in the barrier thickness from 1 to 0.2 μm shifts the responsivity peak from 15 to 10 μm, and also decreases the strength of 7 μm peak. Therefore, by varying the barrier thickness, detectors with different peak positions and single-or two-color responses can be designed.

A detector with broad response can be designed using an *n*-type substrate. The total absorption in structure II with an *n*-type top contact (1×10^{19} cm^{-3}) and an undoped barrier layer grown on a highly doped *n*-type substrate (2×10^{18} cm^{-3}) is presented in Fig. 8(a). This shows a high absorption in a broad spectral range, from 1 to 25 μm. The absorption does not show a strong resonance character since the position of the effective reflection plane changes with wavelength producing a variable phase shift. As a result, the condition for destructive interference at the top contact is satisfied over a broad spectral region. Therefore, the corresponding detector responsivity has a broad bandwidth as shown in Fig. 8(b). The large skin depth in the 2×10^{18} cm^{-3} *n*-doped substrate causes the main absorption inside the substrate leading to a lower response in forward bias configuration.

Structures III and IV are similar to structures I and II, respectively, except for *p*-doped contacts and substrate, and the number of layers. Calculated responsivities of these structures are presented in Fig. 9. Responsivity is higher than for *n*-type structures due to higher internal photoemission probability in *p*-type layers (Fig. 4) and gain from the multiemitters. Furthermore, higher reflectivity due to smaller skin depth of *n*-type layers (see inset of Fig. 9) can be used to increase the absorption in these structures. Structure V in Table I has an *n*-type buffer layer between the bottom contact and the undoped substrate. The buffer layer does not take part in the carrier injection, but contributes to the formation of the standing wave in the structure, increasing the optical electric field in the emitter. As a result, the responsivity would increase as shown in Fig. 9. The reflection from the *n* buffer has increased the responsivity by a factor of ~3. The narrow peak [due to Fabry-Pérot effect at wavelengths defined by Eq. (11)] in the response may be important for special applications such as detecting laser radiation.

To increase the spectral width of the responsivity, structure VI with several emitters can be used. The maximum optical electric field of the standing wave formed inside the structure occurs at different distances from the plane of reflection for different wavelengths. These distances are approximately defined by $\lambda/[4\ \mathrm{Re}(n)]m$, where m is an integer and $m=1,2,3,\ldots$ Therefore, each emitter selectively maximizes the absorption for the corresponding wavelength. This allows the emitters placed at different locations in the structure to contribute photogenerated carriers with the maximum response at different wavelengths. These contributions combine to give a broader photoresponse curve.

Figure 10 shows the absorption spectra for each of the nine emitters of structure VI. The first emitter has a maximum absorption around 10 μm while the ninth emitter has it around 15 μm. The *n*-doped substrate effectively reflects incident radiation of wavelengths greater than 10 μm while allowing shorter-wavelength radiation to penetrate through, producing the main absorption inside the substrate. The absorption in each emitter is less than the absorption in the top and bottom contacts due to the reduced thickness. However, carrier scattering lengths in the emitters are on the order of the emitter thickness, and this leads to a high internal photoemission quantum efficiency. Therefore, the contribution to

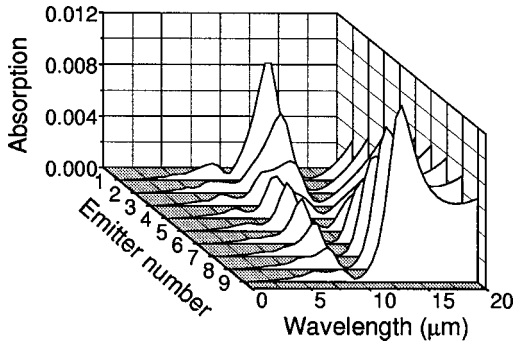

FIG. 10. Calculated absorption in the emitter layers vs wavelength for structure VI. The structure consists of *p*-type top and bottom contacts with a doping concentration of 1×10^{19} cm^{-3} and thicknesses of 400 and 700 nm, respectively. This has nine periods of emitter/barier layers. Emitters (*p* type with the doping level of 3×10^{18} cm^{-3}) are 70 nm thick while barriers (undoped) are 100 nm. The *n*-type substrate has a doping concentration of 1×10^{19} cm^{-3}.

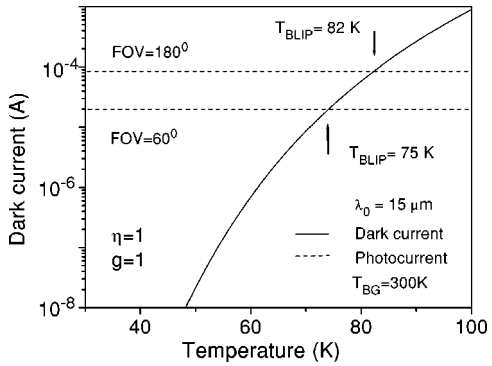

FIG. 12. Calculated temperature dependence of the dark current in HEIWIP structure VI under a bias of 2×10^3 V/cm. The interfacial workfunction corresponds to λ_0 of 15 μm. The photocurrent levels shown by dashed lines at 2.1×10^{-5} and 8.5×10^{-5} A are produced by the $T_{BG}=300$ K background illumination for FOV=60° and 180°, respectively. Quantum efficiency and gain are assumed to be 1. The intersections of the photocurrent levels with the dark current curve yield BLIP temperatures of $T_{BLIP}=75$ K and 82 K for FOV=60° and 180°, respectively.

the photocurrent from the emitters is expected to be high. Absorption in the individual contacts has a resonant character, but the total absorption shows a broad spectral shape. Therefore, the responsivity spectra that include generation in the top or bottom contact, and in the emitters also have broad spectral shape as demonstrated in Fig. 11. The main absorption in structure VI occurs in the bottom contact while the emitters absorb only a small part of the radiation. Significant improvements may be achieved in the forward configuration by replacing the *p*-type bottom contact with an *n*-type layer of the same thickness.

The thermionic dark current of structure VI designed for $\lambda_0=15$ μm ($\Delta=83$ meV) is shown in Fig. 12. Hole mobility was taken as $\mu=60$ cm^2/V s and the electric field as 2×10^3 V/cm. Photocurrents for an ideal detector ($\eta=1$), allowing $g_n=g_p=1$, under the 300 K background illumination with the FOV of 60° and 180° are also presented in Fig. 12. The figure shows that the BLIP regime for an ideal HEIWIP detector should be at temperatures lower than $T_{BLIP}=75$ and 82 K with peak detectivity values of 6.6×10^{10} and 3.3×10^{10} Jones for FOV 60° and 180°, respectively. In reality, η depends on wavelength and has a value lower than unity, which leads to a lower BLIP temperature and a lower detectivity.

Structure VII is designed for a peak response around 22 μm to detect radiation from a quantum cascade laser.[2] A 35 meV ($\lambda_0\simeq35$ μm) interfacial workfunction was chosen to avoid the high reflection region (reststrahlen band) in GaAs. The *n*-type bottom contact serves as both an electric contact and a mirror. Figure 13(a) demonstrates a significant increase in absorption in the emitters. Absorption peaks ($\simeq70\%$) around 24 μm. This leads to an increased peak in

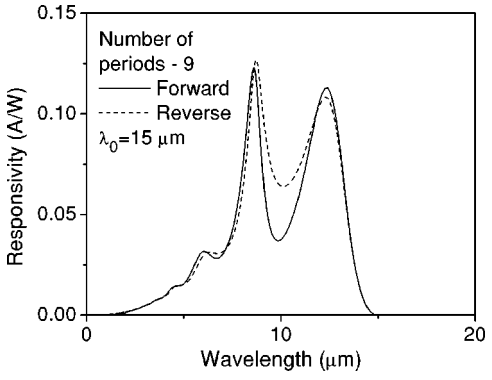

FIG. 11. Calculated responsivity spectra for structure VI having nine periods of emitter/barrier layers. The structure consists of *p*-type top and bottom contacts with a doping concentration of 1×10^{19} cm^{-3} and thicknesses of 400 and 700 nm, respectively. Emitters (*p* type with the doping level of 3×10^{18} cm^{-3}) are 70 nm thick while barriers (undoped) are 100 nm. The *n*-type substrate has a doping concentration of 1×10^{19} cm^{-3}. Forward curve represents the carriers injected from the top contact and from the emitters simultaneously. Reverse curve—from the bottom contact and all the emitters. The interfacial workfunction corresponds to $\lambda_0\sim15$ μm.

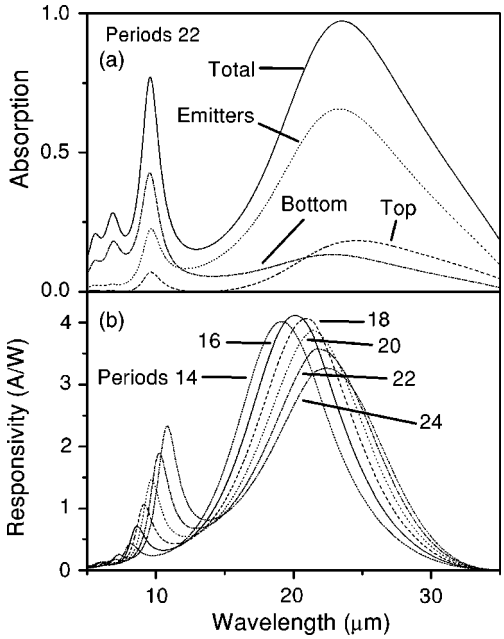

FIG. 13. Calculated total absorption, absorption in the top and bottom contacts, and in the emitters (a) and responsivity spectra (b) in structure VII with 22 periods of emitter/barrier layers. The structure consists of *p*-type top and *n*-type bottom contacts with a doping concentration of 1×10^{19} cm^{-3} and thicknesses of 100 and 700 nm, respectively. Emitters (*p* type with a doping level of 1×10^{19} cm^{-3}) are 30 nm thick while barriers (undoped) are 50 nm. The substrate is SI GaAs and $\lambda_0\sim35$ μm.

response as clearly shown in Fig. 13(b). The variation of the peak position with number of emitter/barrier periods is shown in Fig. 13(b). The increasing number of layers would increase the total thickness of the structure causing the resonance cavity peak to shift towards longer wavelength according to Eq. (11). Meanwhile, the amplitude of the peak response reduces with the thickness. This is due to decreasing internal photoemission probability as the peak moves closer to λ_0.

The thickness of the bottom contact is about three times higher than skin depth of the peak wavelength. Calculation shows that a thinner bottom contact is transparent, and leads to a lower absorption in the structure decreasing the responsivity. As the evanescent wave travels close to three times the skin depth in to the doped layer, increasing the bottom contact thickness beyond that would not be useful. Furthermore, thin structures are economical and easy to grow technologically. The increase in doping concentration decreases the skin depth and the effective total thickness of the structure causing a blueshift of the peak wavelength. Hence, by increasing the number of layers, a tradeoff is achieved, and this would fix the peak wavelength as designed. In other words, this would bring the peak back within the photoemission maximum restoring the designed high responsivity of the detector. According to calculations, for a doping concentration of 2×10^{19} cm^{-3}, the number of layers should be 25. As expected, the responsivity would further increase by 6%, but technological limits may restrict the level of doping concentration.

The experimental and model (without the 28 μm AlAs phonon absorption) responsivity spectra for a HEIWIP detector (sample 2409) are shown in Fig. 14(a). This sample has 30 periods of emitter/barrier layers giving 31 emitters (absorbers). Further details of this sample with experimental and model absorption spectra were published in Ref. 13. Calculations were performed using the responsivity gain as the fitting parameter, giving $g\simeq2$. The estimated capture probability was $p_c=1/Ng\simeq0.02$, close to the value for QWIP structures.[18] Responsivity can be increased by using an *n*-type substrate with a doping concentration of $\sim10^{18}$ cm^{-3}. In practice, it is difficult to produce high quality substrates with doping concentrations higher than 10^{18} cm^{-3}. However, molecular beam epitaxy and metal-organic chemical-vapor deposition techniques permit the growth of doped epilayers up to concentrations $\sim10^{19}$ cm^{-3} to serve as reflecting layers.

Model responsivity spectra for structures similar to 2409 are shown in Fig. 14(b). The 1.5 μm thick *n*-type buffer layer between the *p*-type bottom contact and the substrate increases the responsivity by ~1.7 times while the *n*-type bottom contact increases it by ~2 times. The responsivity could be further increased (~4.5 times) by increasing the emitter doping concentration up to 1×10^{19} cm^{-3}. However, it should be noted that high doping in emitters may increase the dark current.

Finally, the model for structure 2409 agrees well with the experimental result [see Fig. 14(a)] indicating that the model well describes the main features of carrier generation and the emission over the barrier. Therefore, the model could be used to design and optimize HEIWIP devices.

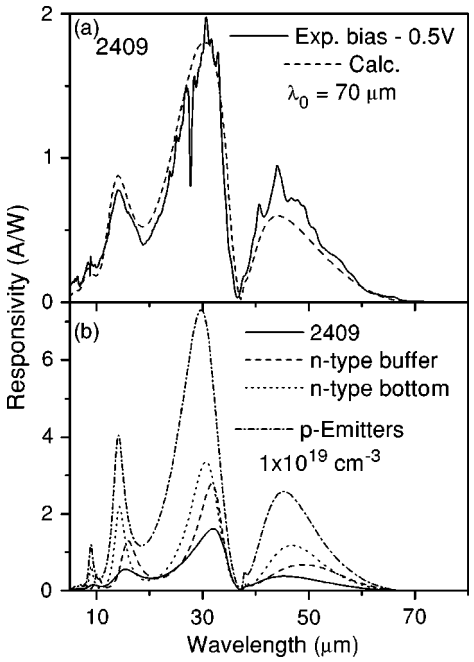

FIG. 14. (a) Experimental and calculated responsivity spectra for structure 2409 (Ref. 13). The structure has 30 periods of emitter/barrier layers. The carrier concentration in the top and bottom contacts is 2.4×10^{19} cm^{-3}. Emitters have a doping level of 2×10^{18} cm^{-3}. Thicknesses of the top contact, barriers, emitters, and bottom contact are 208, 77, 15, and 730 nm, respectively. The total thickness of the structure is 3.5 μm. The responsivity of optimized structure is shown in (b). The responsivity would be increased 1.7, 2.1, or 4.5 times by including an *n*-type buffer layer, *n*-type bottom contact, or by increasing emitter doping concentration, respectively.

IV. SPECIFIC DETECTIVITY

Model specific detectivity D^* spectra of HEIWIP detector 2409 in the BLIP regime is presented in Fig. 15. The calculated BLIP temperature was $T_{\mathrm{BLIP}}=13$ K for a background temperature of $T_{\mathrm{BG}}=300$ K and a FOV of 180°. The figure demonstrates a peak D^* of 1.7×10^{10}, 2.4×10^{10}, 2.5

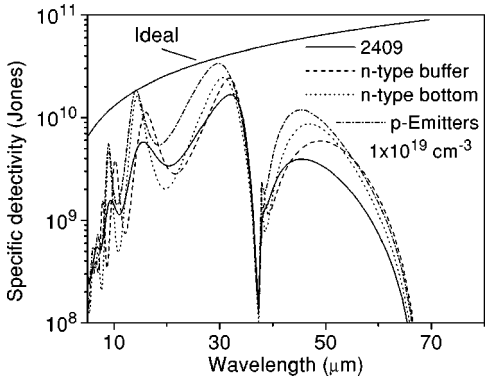

FIG. 15. The solid line shows calculated detectivity spectra for 2409 HEIWIP detector in the BLIP regime (λ_0 is 70 μm). Background temperature is $T_{\mathrm{BG}}=300$ K and FOV=180°. The BLIP temperature is $T_{\mathrm{BLIP}}=13$ K. Model detectivities of structures similar to 2409, but with a 1.5 μm thick *n*-type buffer layer doped to 1×10^{19} cm^{-3}, an *n*-type bottom contact, or emitter concentration increased to 1×10^{19} cm^{-3} are shown for comparison. The top solid line represents the detectivity of an ideal detector with the same λ_0.

$\times 10^{10}$, or 3.4×10^{10} Jones for detector 2409, if an *n*-type buffer layer, *n*-type bottom contact, or highly doped *p*-type emitters are used, respectively. The D^* for an ideal detector with the same $\lambda_0 = 70$ μm is also shown in the figure.

V. DETECTOR TIME RESPONSE

Mainly, there are three mechanisms limiting the response time of HEIWIP detectors.

A. Intrinsic time response

The intrinsic time response of a *p*-GaAs/AlGaAs HEIWIP detector can be estimated from the bias dependent responsivity measurements.[20] Under radiation, excited carriers are generated by free carrier absorption in the valence band. However, the total number of carriers remain constant with an effective temperature T_{eff} (deviated from equilibrium temperature T_0) in a hot-carrier population. The photoconductivity is given by

$$\Delta\sigma = qp[\mu(T_{\text{eff}}) - \mu(T_0)], \tag{12}$$

where p is carrier concentration and μ is the hole mobility. As $I_{\text{photo}} = \Delta\sigma FA$, the change in conductivity under illumination changes the current (photocurrent) through the external circuit. Here, F is electric field in the detector and A is the area. For a negligible heating of the carriers

$$\Delta\sigma = qp \left.\frac{d\mu}{dT}\right|_{T=T_0} (T_{\text{eff}} - T_0). \tag{13}$$

Therefore, the photoconductivity is directly related to the transport properties of the hot carriers. The temperature increase from T_0 to T_{eff} is related to the incident power P through the energy balance equation

$$\frac{pk(T_{\text{eff}} - T_0)}{\tau} = \frac{P\eta}{Ad}, \tag{14}$$

where k is Boltzmann's constant, d is detector thickness, and τ is the energy relaxation time of the hot carriers, which in the limit can be regarded as the detector response time. The left term in Eq. (14) represents the power transferred to the lattice by the hot carriers while the right term corresponds to the power transferred to the hot-carrier distribution. The current responsivity $R = I_{\text{photo}}/P$ under a bias voltage V can be expressed as

$$R = \frac{q\eta\tau}{kd^2} \left.\frac{d\mu}{dT}\right|_{T=T_0} V. \tag{15}$$

Using the temperature dependent mobility $\mu \propto T^{3/2}$, due to the ionized impurity scattering for the low experimental temperature of $T_0 = 4.2$ K the current responsivity can be rewritten as

$$R = \frac{3\eta\mu\tau}{2d^2}\frac{q}{kT_0}V. \tag{16}$$

The bias dependence of responsivity measured at 4.2 K in a *p*-GaAs HEIWIP FIR detector with 30 periods of emitter/barrier layers and λ_0 around 70 μm is shown in Fig. 16. The measured responsivity increases linearly with the bias at low bias voltages as predicted by Eq. (16). The saturation of the responsivity at high bias is due to the quasi-depletion of the impurity band as proposed in a simple recombination model.[21] For a given bias, the responsivity is proportional to the response time, which is the same as in the case of intrinsic or extrinsic photoconductive detectors. The detector 2409 has a total absorption quantum efficiency of 0.07 at 14 μm and a slope of 0.78 A/W V in the linear region of R vs V graph in Fig. 16. Using the above parameters the response time of this detector, determined by the energy relaxation time, is estimated to be $\tau_{\text{relax}} \cong 6\times 10^{-12}$ s.

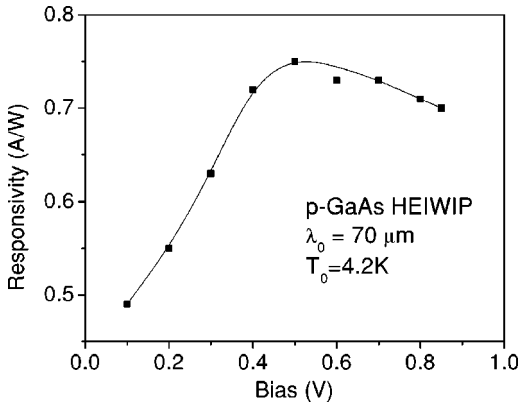

FIG. 16. Bias dependence of responsivity for 2409 HEIWIP detector with 30 periods of emitter/barrier layers with a λ_0 of 70 μm.

B. Transit time

Assuming the hole mobility to be $\mu = 60$ cm^2/V s, the transit time of the carrier through this structure, at an electric field of 3 kV/cm, was estimated to be $\tau_{\text{trans}} \cong 10^{-9}$ s.

C. *RC* time constant

In practice, the most serious limitation arises from $\tau_{RC} = R_{\text{total}}C$ constant, where C is capacitance of the detector and $R_{\text{total}} = R_L R_d/(R_L + R_d)$ is the equivalent resistance. Here, R_L is load resistance and R_d is the dynamic resistance of the detector. Typical values for R_d of a HEIWIP detector with a cutoff $\lambda_0 = 70$ μm is about 5×10^5 and 5×10^4 Ω for a bias of 0.5 and 0.7 V, respectively.

The capacitance for a 3 μm thick detector with a 400×400 μm^2 elctrical area is about 6 pF. For an extremely high load resistance ($R_L \gg R_d$) the *RC* time constant is estimated to be 3×10^{-7} s. Increasing the electrical area of the detector to 800×800 μm^2 increases the time constant to 1.2×10^{-6} s.

As a result, the intrinsic time response of the HEIWIP detectors is high, and in real situations detector time response is restricted by the *RC* time constant.

VI. CONCLUSION

In summary, the principles of modeling, designing, and optimizing the performance of GaAs/AlGaAs HEIWIP IR detectors of different types are considered. It is shown that different types of HEIWIP detectors for different spectral ranges may be designed through proper combinations of *n*-

and *p*-type layers. Responsivity may be improved by using a highly reflecting *n*-type buffer layer between the bottom contact and the substrate. The position of the peak responsivity and spectral width may be varied by adjusting the thickness of the emitter and barrier layers. It is shown that a *p*-type emitter is more effective compared to *n* type due to its higher internal photoemission. However, *n* type is more effective as a reflector inside the structure for enhanced cavity effect. The detectors with multiemitter structures give higher responsivity and a broader spectral response due to effective emission from all the thin emitters. Maximum response can be achieved in the structure with *p*-type top and *n*-type bottom contacts through a significant increase of the optical electric field in the emitters. Finally, the time response of HEIWIP detectors is not restricted by the intrinsic processes, but by their *RC* time constants.

ACKNOWLEDGMENT

This work was supported in part by the NSF under Grant No. ECS-0140434. M. B. M. Rinzan is supported by GSU RPE funds. Authors acknowledge fruitful discussion with Dr. H. C. Liu at National Research Council, Canada.

[1]G. L. Pilbratt, in *The Herschel Mission, Scientific Objectives, and this Meeting*, The Promise of the Herschel Space Observatory (ESA, The Netherlands, 2001), pp. 13–20.
[2]R. Colombelli *et al.*, Appl. Phys. Lett. **78**, 2620 (2001).
[3]E. E. Haller, Infrared Phys. Technol. **35**, 127 (1994).
[4]D. M. Watson, M. T. Guptill, J. E. Huffman, T. N. Krabach, S. N. Raines, and S. Satyapal, J. Appl. Phys. **74**, 4199 (1993).
[5]J. E. Huffman, A. G. Crouse, B. L. Halleck, T. V. Downes, and T. L. Herter, J. Appl. Phys. **72**, 273 (1992).
[6]A. G. U. Perera, S. G. Matsik, B. Yaldiz, H. C. Liu, A. Shen, M. Gao, Z. R. Wasilewski, and M. Buchanan, Appl. Phys. Lett. **78**, 2241 (2001).
[7]S. G. Matsik, M. B. M. Rinzan, A. G. U. Perera, H. C. Liu, Z. R. Wasilewski, and M. Buchanan, Appl. Phys. Lett. **82**, 139 (2003).
[8]S. G. Matsik, M. B. M. Rinzan, D. G. Esaev, A. G. U. Perera, H. C. Liu, and M. Buchanan, Appl. Phys. Lett. **84**, 3435 (2004).
[9]A. G. U. Perera, in *Semiconductor Photoemissive Structures for Far Infrared Detection*, Handbook of Thin Film Devices Frontiers of Research, Technology and Applications, Semiconductor Optics, Vol. 2, edited by M. H. Francombe, A. G. U. Perera, and H. C. Liu (Academic, New York, 2000), pp. 135–169.
[10]M. S. Unlu, G. Ulu, and M. Gokkavas, in *Resonant Cavity Enhanced Photodetectors*, Photodetectors and Fiber Optics, edited by H. S. Nalwa (Academic, New York, 2001), pp. 97–201.
[11]J. S. Blakemore, J. Appl. Phys. **53**, R123 (1982).
[12]M. V. Klein and T. E. Furtac, *Optics* (Wiley, New York, 1986).
[13]D. G. Esaev, S. G. Matsik, M. B. M. Rinzan, A. G. U. Perera, H. C. Liu, and M. Buchanan, J. Appl. Phys. **93**, 1879 (2003).
[14]A. G. U. Perera, H. X. Yuan, and M. H. Francombe, J. Appl. Phys. **77**, 915 (1995).
[15]V. E. Vickers, Appl. Opt. **10**, 2190 (1971).
[16]J. M. Mooney and J. Silverman, IEEE Trans. Electron Devices **32**, 33 (1985).
[17]M. J. Kane, S. Millidge, M. T. Emeny, D. Lee, D. R. P. Guy, and C. R. Whitehouse, in *Intersubband transitions in Quantum Wells*, edited by E. Rosenchenr, B. Vinter, and B. Levine (Plenum, New York, 1992).
[18]H. C. Liu, Appl. Phys. Lett. **61**, 2703 (1992).
[19]M. Ershov and H. C. Liu, J. Appl. Phys. **86**, 6580 (1999).
[20]W. Z. Shen and A. G. U. Perera, Infrared Phys. Technol. **39**, 329 (1998).
[21]W. Z. Shen, A. G. U. Perera, S. K. Gamage, H. X. Yuan, H. C. Liu, M. Buchanan, and W. J. Schaff, Infrared Phys. Technol. **38**, 133 (1997).